MAPPING EXTINCTION IN NEARBY GALAXIES

University of La Laguna

Eduardo Alberto Mantero Castañeda

Supervised by Dr. Johan Knapen
and Dr. Fatemeh Tabatabaei

Science Faculty ULL, Master in Astrophysics
edumantero94@gmail.com
June. 2018

I. Resumen

El estudio de las galaxias y sus componentes nace en los tiempos de los griegos, cuando empezaron a preguntarse por la composición de la banda luminosa del cielo conocida como la Vía Láctea. Este estudio ha ido evolucionando con el paso de las épocas hasta llegar a la actualidad, donde la astrofísica galáctica y extragaláctica forman grandes campos de investigación. Dentro de ellos, el estudio del medio interestelar y sus componentes cobra una gran relevancia debido a que este medio es una de las partes más importantes de una galaxia.

En este trabajo nos centraremos en el estudio de uno de los componentes más importantes del medio interestelar, el polvo. La importancia del mismo no radica en la cantidad presente en las galaxias sino en su interacción y efectos que produce en la luz que lo atraviesa. El polvo, principalmente, produce extinción en la luz provenientes de las estrellas de una galaxia a través de la absorción y difusión de la misma, siendo mayor la extinción en longitudes de onda más pequeñas. Con este estudio, buscamos realizar mapas de extinción de galaxias cercanas y estudiar como varía esta dentro de ellas. Además, utilizaremos los mismos datos para estudiar los flujos de las regiones HII de dicha galaxia en longitudes de onda de Hα y Hβ y con ello, obtendremos también la tasa de formación estelar de distintas zonas en el interior de la galaxia.

Los datos utilizados para cumplir dichos objetivos han sido tomados en los proyectos 20170109 y 20170110, utilizando el telescopio William Herschel (4.2 m) en la Palma, con la cámara ACAM con un campo de visión de 8 arcmin. Se tomaron imágenes de la galaxia NGC628 y NGC5194 durante las noches del 9 y 10 de enero del 2017 usando cuatro filtros estrechos distintos, dos de ellos conteniendo las líneas de emisión estudiadas (Hα y Hβ) y los otros dos el continuo de la galaxia cercano a las mismas. Debido a un problema con los filtros durante las noches de observación, no se han podido utilizar las imágenes de la galaxia NGC5194 para nuestro estudio, con lo que nos centraremos principalmente en el estudio de NGC628.

Las imágenes de la galaxia fueron reducidas utilizando IRAF [2] siguiendo el procedimiento habitual para este tipo de imágenes salvo por la calibración de las mismas. El "bias" fue substraído de todas las imágenes usando los "overscans" presentes en cada una de ellas, seguidamente, se corrigieron de "flat-field" utilizando para ello las imágenes tomadas en las noches de observación para cada filtro y tras esto, fueron combinadas todas las imágenes de un mismo filtro para aumentar el cociente entre la señal y el ruido de la imagen. Al tener distintos "seeings" por ser imágenes provenientes de distintas noches de observación, cada imagen fue suavizada para igualar el "seeing" de la peor y con ello poder comparar las imágenes entre sí. El siguiente paso consistió en la substracción del continuo de la galaxia para obtener así una única imagen para cada línea de

emisión. Finalmente, estas imágenes fueron calibradas en flujo, pero debido a un problema con los datos para la calibración tomados esas noches, decidimos realizar una calibración cruzada con datos obtenidos de la bibliografía, en concreto de Sánchez et al. (2010) [25]. Tras esta calibración obtenemos el factor de escala para tener nuestras imágenes en unidades apropiadas. Con lo que el resultado del proceso de reducción son dos imágenes, una de cada línea de emisión (Hα y Hβ) de la galaxia NGC628.

Partiendo de la expresión del transporte radiativo, calculamos el coeficiente de extinción utilizando para ello la curva de enrojecimiento usual para estudios extragalácticos extraída de Calzetti et al. (2000) [5]. Con esto podemos calcular el mapa de extinción de la galaxia. Además, también obtenemos la expresión para corregir de dicha extinción los flujos obtenidos de las imágenes para cada línea de emisión. Finalmente obtendremos la expresión para la tasa de formación estelar siguiendo a Kennicutt et al. (1980) [17], utilizando para ello el flujo en la línea de emisión de Hα corregido de extinción.

Utilizando las expresiones comentadas, calculamos el mapa de extinción para la galaxia NGC628, el mapa obtenido presenta un coeficiente de extinción medio de $A_V = 0.98 \pm 0.62$, siendo este resultado comparable con otros valores encontrados en la bibliografía. Aunque, debido a que el mapa no presenta mucha información en gran parte de la galaxia (causado por los problemas con la imagen para Hβ), decidimos estudiar distintas regiones HII de la galaxia para poder estudiar más en detalle la extinción en distintos puntos de la misma. Para ello, seleccionamos 38 regiones HII repartidas por la galaxia. De estas regiones obtenemos los flujos en ambas líneas de emisión, también la extinción y la tasa de formación estelar presentes en ellas. La media de extinción en este caso es de $A_V = 1.54 \pm 0.62$, sigue siendo un valor comparable a los encontrados en la bibliografía aunque mayor que el obtenido en el mapa de extinción. Esta discrepancia esta debida principalmente a que en el mapa de extinción, solo tenemos información de las partes exteriores a las regiones HII donde el coeficiente de emisión es menor mientras que en la tabla calculamos la extinción principalmente en regiones de los brazos espirales donde la extinción suele ser mayor. Los flujos obtenidos son comparables y en algunos casos idénticos a otros encontrados en la bibliografía. La tasa de formación estelar varía entre 0.003 y 0.116 [$M_\odot$/yr] siendo esta variación lo usual para esta galaxia (Gusev et al. 2015 [14]), además encontramos la existencia de un máximo en la tasa de formación a una distancia del centro similar a otras distancias comentadas en otros artículos para el mismo máximo. La tasa de formación estelar para la galaxia es de 0.9 [$M_\odot$/yr], un valor menor al encontrado en otros artículos debido a que no hemos considerado todas las regiones existentes en la galaxia.

Concluimos este trabaja comentando la posibilidad de obtener este tipo de mapas de extinción utilizando metodos de imagen, donde el detalle de los mismos está limitado a la dificultad para obtener imágenes en Hβ usando la fotometría tradicional, y dándonos cuenta de que resulta más sencillo estudiar regiones HII por separado que estudiar flujos píxel por píxel en las imágenes.

II. Abstract

The study of galaxies and their composition was born in the times of the Greeks, when they began to wonder about the composition of the luminous band of the sky known as the Milky Way. This study has evolved with the passage of the epochs until arriving at the present time, where the galactic and extragalactic astrophysics form great fields of investigation. Among them, the study of the interstellar medium and its components takes on great relevance because this medium is one of the most important parts of a galaxy.

In this work, we will focus on the study of one of the most important components of the interstellar medium, dust. The importance of it does not lie in the amount present in the galaxies but in their interaction and effects that it produces in the light that crosses it. The dust absorbs and scatters the light coming from the stars in a galaxy, it mainly absorb the light at wavelengths similar or smaller than their size. Both process produce extinction. In this study, we seek to map extinction in nearby galaxies and study how it varies within them. In addition, we will use the same data to study the HII regions fluxes of the galaxy at wavelengths of Hα and Hβ. And with this, we will also obtain the star formation rate of different zones in the interior of the galaxy.

The data used to meet these objectives have been taken under the projects 20170109 and 20170110 using the William Herschel telescope (4.2 m) on La Palma, with the ACAM camera with an 8 arcmin field of view. Images of the galaxies NGC628 and NGC5194 were taken during the nights of January 9^{th} and 10^{th}, 2017 using four different narrow filters, two of them containing the emission lines studied (Hα and Hβ) and the other two the continuum of the galaxy close to them. Due to a problem with the filters during the observation nights, we have not been able to use the images of the galaxy NGC5194 for our study, hence we will focus mainly on NGC628.

The raw data of the galaxy were reduced following the standard procedures in IRAF [2] except for the calibration. The bias was subtracted from all the images using the overscans present in each of them. Then, they were corrected from flat-field using the images taken during the observing nights for each filter and after that, all the images of the same filter were combined to increase the quotient between the signal and the noise of the image. As the images were observed under different seeing conditions, each image was smoothed to match with image with worst seeing in order to compare them with each other. The next step consisted of subtracting the galaxy's continuum to obtain a single image for each emission line. Finally, these images were calibrated in flux using a cross-calibration with data obtained from the bibliography, specifically Sánchez et al. (2010) [25]. After this calibration we obtain the scale factor to have our images in appropriate units. The result

of the reduction process were two images, one for each emission line (Hα and Hβ) of the NGC628 galaxy.

Starting from the expression of radiative transport, we calculated the extinction coefficient using the usual reddening curve for extragalactic studies extracted from Calzetti et al. (2000) [5]. With this we can calculate the extinction map of the galaxy. In addition, we also obtain the equation to correct the integrated fluxes for extinction for each emission line. Finally we will obtain the rate of massive star formation following Kennicutt et al. (1980) [17], using the flux in the Hα emission line corrected of extinction.

Using the obtained relations, we calculated the extinction map for the galaxy NGC628, the obtained map presents a mean extinction of $A_V = 0.98 \pm 0.62$, this result is comparable with other values found in the bibliography. Although, because the map does not present much information in many parts of the galaxy (due to the sensitivity of the image for Hβ), we decided to study different HII regions of the galaxy in order to study in more detail the extinction in different points of the image. For this, we selected 38 HII regions distributed throughout the galaxy. From these regions we obtain the fluxes in both lines of emission, also the extinction and the star formation rate. The mean extinction in this case is $A_V = 1.54 \pm 0.62$, it is still a value comparable to those found in the bibliography, although higher than the obtained in the extinction map. This discrepancy is mainly due to the fact that in the extinction map, we only have information from parts outside the HII regions where the emission coefficient is lower while in the table we calculate the extinction mainly in regions of the spiral arms where the extinction is usually greater. The fluxes obtained are comparable and in some cases identical to others found in the bibliography. The star formation rate varies between 0.003 and 0.116 [$M_\odot$/yr] being this variation the usual for this galaxy (Gusev et al. 2015 [14]), we also find the existence of a maximum in the star formation rate at a distance from the centre similar to other distances discussed in other articles for the same maximum. The rate of star formation for the galaxy is 0.9 [M_*odot*/yr], a value lower than that found in other articles because we have not considered all the existing regions in the galaxy.

We conclude this work commenting that it is possible to obtain this kind of extinction map using just imaging methods and the detail of them is limited to the difficulty to obtain the Hβ image using the traditional photometry.

Contents

CHAPTER 1

Introduction

The interest in the study of galaxies and their composition can be found from very early in the beginning of philosophical thought. It was in the 5^{th} century BC. when Democritus (460-370 BC.), for the first time, proposed that the bright band in the night sky known as the Milky Way, could be composed of many stars. This was, probably, the first mention of the composition of a galaxy. Of course that was only a supposition without an experimental observation, something common in that epoch.

We had to wait until the XVIIth century, when Galileo Galilei (1564-1642) in 1610 used his telescope to confirm that the Milky Way was made of stars. Later, in 1750, Tomas Wright (1711-1786) described the shape of the Milky Way and speculated that the nebulae that were observed in the night sky were other distant galaxies different from the Milky Way. In 1755, Immanuel Kant used the term "Island Universe" to describe these distant nebulae. After this, some astronomers started thinking that many of the nebulae were, indeed, other galaxies. This thought was accentuated later in 1845 by William Parsons (1800-1867) who discovered a spiral "nebula" (currently know as the Whirlpool Galaxy, M51) and many others with a similar shape to the Milky Way. All this led to the great debate, in 1920, between Harlow Shapley (1885-1972) and Heber Curtis (1872-1942) about the nature of the spiral "nebulae" and the size of the Universe. This debate was closed by Edwin Hubble (1889-1953) when he discovered a Cepheid in the Andromeda "Nebula" which let him measure the distance to it and know that it was outside the Milky Way. From this discovery on, it was renamed as The Andromeda Galaxy, probing the existence of other galaxies and the possibility, checked after this, that the spiral nebulae are indeed galaxies.

Nowadays the existence of galaxies is undeniable, and we know that they are a gravitationally bound system of stars, stellar remnants, interstellar medium, and dark matter. In this work we will study one of the fundamental components of the interstellar medium in galaxies, the dust and its effects on the light that emits from the galaxies.

1.1 Interstellar Medium

The interstellar medium (ISM) is named to the matter and energy that exist in the space between the stars in a galaxy. It is the primary galactic repository out of which stars are born and into which they deposit energy, momentum and enriched material as they die. It constitutes the anchor point of the galactic matter cycle, and as such is the key to a consistent picture of galaxy formation and evolution. Components of the interstellar medium are gas, dust, cosmic rays and the interstellar magnetic field and radiation field.

The gas in the ISM is composed almost entirely of hydrogen and helium, with hydrogen accounting for around 70% of the total mass, helium for 28%, and all other elements for the remaining 2% (Klessen 2014) [19]. The thermal and chemical state of the ISM is conventionally described in terms of a number of distinct phases. The dense molecular gas, the cold neutral medium, the warm neutral medium, the warm ionized medium and the hot ionized medium. All these phases have different temperature, density and ionization.

The dust is responsible for absorbing light over a wide range of frequencies causing reddening of starlight in the ISM. To a first approximation, individual dust grains absorb only those photons with wavelengths smaller than the physical size of the grain. Therefore, the fact that we see a large amount of absorption in the ultraviolet, somewhat less in the optical and even less at infrared wavelengths tells us immediately that there are many more small dust grains than there are large ones. The dust is just around an 1 % of the total mass of the ISM.

The cosmic rays are relativistic particles (electrons, positrons and nucleons) from a wide range of energies, so the cosmic rays play an important role in the overall energy balance of the gas. The spectrum of the cosmic rays decreases sharply with increasing energy, and so the majority of the heating and ionization that they provide comes from the least energetic cosmic rays.

Finally, the interstellar radiation field is named to all the electromagnetic radiation that occupies the same volume in the galaxy, this includes a wide range of wavelengths. From the cosmic microwave background, almost perfect black-body spectrum with a given temperature that can play a significant role regulating the thermal evolution of the gas and dust, to the starlight (essentially visible and soft ultraviolet wavelengths) however, in neutral regions, stellar photons with energies greater than the ionization energy of hydrogen, 13.6 eV, are largely absent as this energy is absorbed by the hydrogen atoms ionizing them and cannot penetrated into this regions. The infrared and far infrared radiation is included in this radiation field too, this radiation is emitted by the dust grains in the form of thermal emission and dominates the spectrum in this region.

The existence of all these components in the interstellar medium, and the psychics which is behind all of them, produce a complicated heating and cooling process in the medium. The gas can be heated by many different physical processes such as the photoionization, the x-ray removing electrons from the atoms and cause a secondary ionization, the cosmic rays that can penetrate deep in the molecular clouds and transfer energy to the gas, the stellar winds, supernova explosions etc. Other heating processes related with the dust in a galaxy are the photoelectric heating by grains, that is produced due to the ultraviolet radiation from hot stars that can remove electrons from the dust grains, these electrons are ejected from the grains and heats the gas through collisions with other particles. And the grain-gas heating, that is occurred when the grains, in high density regions of the galaxy, transfer thermal energy to the gas by collisions.

The main cooling mechanism that occurs in galaxies are cause by the fine structure transitions, which is more efficient in those atoms that have the fine structure levels close to the fundamental, collisions will excite those atoms to higher levels, then, the will de-excite emitting a photon that carries the energy out of the region. And the cooling by permitted lines, where more levels than the fine structure levels are populated via collisions and then, again, it will de-excite emitting a photon that can leave the region, cooling the medium.

1.2 Dust in Galaxies

The dust is an important component of a galaxy, this is not because of its mass (the dust is just an tiny part of the galaxy's mass) but its interaction with the light that comes from the stars and nebulae and its role in the interstellar medium heating and cooling processes.

Cosmic dust consists of tiny particles of solid material floating around in the space between the stars, the size and form of the particles vary a lot but to be considered as dust particles they have to be smaller than 30 μm, (this limit comes from the consequence of the definition of meteoroid, (IAU 2017) [16]). It gets a different name depending of where the dust is found and we can distinguish intergalactic dust, interstellar dust, interplanetary dust and circumplanetary dust. Dust grains are formed in rapidly cooling gas of stellar outflows caused by Asymptotic Giant Branch stars (AGB), supernovae, red supergiants, novae Wolf-Rayet stars, and so on, (Gehrz 1989) [12]. Dust abundance is directly connected with galaxy growth through the formation of new stars, the burst contains a significant fraction of the interstellar heavy elements, produced by the process mentioned before, so it plays an important role in the cooling of the interstellar medium through collisionally excited fine structure transitions.

The interstellar dust obscures all but the relatively nearby regions at the visual and ultraviolet wavelengths and re-radiates the absorbed energy in the far-infrared part of the spectrum. This obscuring is known as extinction, and it is caused principally by two physical properties the absorption and scattering. The absorption of the electromagnetic radiation

is not produced only by dust, as the gas that is present in the interstellar medium affect the absorption in a similar way. The light that comes from stars in the galaxy is taken up by matter. The electrons of the gas and dust molecules absorb part of the radiation and then re-radiate it in other directions and other wavelengths causing that in a line of sight we detect less radiation than what it was produced in the star. We can define the scattering of any electromagnetic radiation as the process where the radiation is forced to deviate from a straight trajectory due to localized non-uniformities in the medium. In the interstellar medium, the light of the stars is forced to deviate from the line of sight because of the presence of the dust and gas in the medium.

1.2.1 Extinction Curve

The interstellar extinction of starlight is the most indicative phenomenon revealing the presence of diffuse dark gas in the interstellar medium. The extinction is selective, it is greater in the blue than in the red spectral range. This is why the word "reddening" is often considered synonymous to extinction. Extinction has often been analyzed using a two-colour normalization of the form $E(\lambda-V)/E(B-V)$, however (following Cardelli 1989 [6]) the true nature of the variability of observed extinction may be hidden by the choice of normalization so the quantity $A(\lambda)/A(V)$ is a more fundamental extinction law.

There are different methods to determinate the extinction curve of a star. The pair method, the colour-colour method and the excess-excess method (Krelowski 1993 [21]) are often used. Essentially, the first method consist of compare the flux distribution of a reddened star with an unreddened of the same spectral type and luminosity class. The second method is comparing a set of different stars with the same spectrum and luminosity, in absence of extinction plotting the colour for a given wavelength $(\lambda - V)$ vs. the colour $(B - V)$ should have a single point for all the stars, but with extinction we will obtain a linear relation and we can derive the mean extinction curve of a sample from the slopes of its two-colour relations. The third method is based on the determinations of individual colour excesses from photometric or spectrophotometric data for stars of the same aggregated and correlating the calculated $E(\lambda-V)$ excesses with $E(B-V)$. The linear relations between any pair of colour excesses lead to the mean extinction curve for the whole aggregate.

To get the extinction curve for a whole galaxy, the usual method is to select a sample of stars in different lines of sight and calculate the colour excess with one of the methods mentioned above and then obtain an average of all the extinction curves. The use of different methods to obtain the extinction curve and even the use of different star samples produce different curves. An easy way to compare all this curves is the total to selective extinction ratio, usually expressed as $R_V = A_V/E_{B-V}$, this value is related with the size of the dust grains as we will address later. Different authors have calculated different extinction curves for the milky way diffuse ISM ($R_V = 3.1$) and the dense ISM ($R_V = 5.0$), Cardelli 1989 [6]. For the Large ($R_V = 3.41$) and Small (R_V=2.74) Magellanic Cloud, Gordon 2003 [13]. And

a general extra-galactic extinction curve ($R_V = 3.1$), Calzetti 2000 [5]. We will consider the last one in Chapter 2 because is important for our work.

1.3 Messier 74, The Phantom Galaxy (NGC 628)

Messier 74 (also known as NGC 628) is a spiral galaxy discovered by Pierre Méchain in 1780. It is the brightest member of the M74 Group, a small group of 7 galaxies in the Pisces constellation (RA: 01h43m, DEC:+14º 22') [11]. This galaxy is localized at a distance between 7.7 and 9.7 Mpc from the Milky Way Galaxy [15], we will assume the 9.7 Mpc of distance as our distance to the galaxy because it is the more common value used in the bibliography. This distance was calculated thanks to a type II-P supernova using the standard candle method, for this type of supernovae and it was the first Type II supernova to have a directly confirmed red supergiant progenitor.

Morphologically classified as an Sbc, the galaxy appears face-on and occupies an area of 10.5 by 9.5 arc minutes of apparent sky. It is a perfect example of a grand design spiral galaxy. It has two clearly defined spiral arms, one prominent spiral arm to the south, and one or several disturbed spiral arms to the north, that contains clusters of young blue stars and many starforming regions. Results from a detailed kinematic analysis of the galaxy (Fathi et al. 2007 [8]) showed that the velocity dispersion of the gas for individual H_{II} regions is practically constant at all galactocentric distances and the star formation is widely distributed within the disc so this suggest that that the emission in Hα from the H_{II} regions dominates any emission from the diffuse component.

Figure 1.1: *False colour image of M74 obtained by the combination of three different filters from the data used in this work.*

Another interesting thing in this galaxy was found in the X-ray Chandra observations [7], a source that radiates 10 to 1000 times more X-rays than neutron stars and stellar black holes. This provides evidence that the X-radiation was produced by a black hole of 10000 Solar masses, indicating that it belongs to a possible new class of black holes, intermediate mass black holes, (Koliopanos, 2018) [20].

1.4 Objectives

In this work we will use narrow band imaging from the William Herschel Telescope obtained in the projects 20170109 and 20170110 to obtain an detailed emission map of Hα and Hβ fluxes of the galaxy M74 (NGC 628) to fulfill the following objectives:

- Assess the possibility of obtaining a detailed extinction map of NGC 628 using an imaging method to correct for extinction the future images of this galaxy.
- Obtain the fluxes of Hα and Hβ corrected by dust in different parts of the galaxy.
- Obtain the star formation rate of the whole galaxy and detailed parts of it.

CHAPTER 2

Observations

To achieve the objectives mentioned in the previous chapter we have taken images of the galaxy M74 and M51 with the William Herschel Telescope in La Palma using ACAM (Auxiliary Camera of the telescope) in imaging mode. This camera has a circular field of view with a diameter of 8.3 arcmin. The scale is approximately 0.25 arcsec/pixel (measured on-sky to be 0.253 in x, 0.254 in y, through an R-band filter).

The images were taken on the nights of January 9^{th} and 10^{th} of 2017 during most of a gray night. The seeing of the images vary in different nights between 1.05 arcsec and the worst of 1.8 arcsec. Because our main intention was to obtain an extinction map of the galaxy M74 and M51, we chose to observe in Hα and Hβ lines and we chose the following filters to do our observations:

Filter	**Central Wavelength [Å]**	**FWHM [Å]**	**Throughput Peak [%]**
T4550	4550	100	55
T4880	4880	100	68
T6590	6590	130	57
T6770	6770	50	50

Table 2.1: *Filters used in this work and their characteristics, taken from the ING filter database search.*

Taking into account that for Hα and Hβ the wavelengths of this emission lines are 6563 Å and 4861 Å respectively, we have a filter for each line that contains that line and another filter for each line that is close to the previous filter but does not contain the line but the

galaxy's continuum. This is for the continuum subtraction of the galaxy that we will see in Section 2.1.4.

For each filter, we have taken different numbers of images for both galaxies with different exposition times. In the next table we can see the exposition times M74 galaxy:

Filter	**Number of images**	**Exposure time [s]**	**Total Integrated time [s]**
T4550	2	900	1800
T4880	3	900	2700
T6590	20	60	1200
T6770	12	200	2400

Table 2.2: *Exposure time for the images of M74 for the different filters.*

For each of these images we have applied a reduction process that we will describe in the next section.

Problems with M51

Although images were taken for both galaxies (M74 and M51) and in principle both galaxies were going to be studied in this work, due to a problem during the observation nights with the Hα and Hβ filters, part of the images of both objects were completely useless for this study, luckily, for M74 we managed to obtain images for all the filters combining the two observation nights. On the other hand, for the M51 galaxy, no useful images were obtained in several filters, which made this study with this galaxy impossible. Therefore, we will only focus on the galaxy of M74 and discuss the reduction process only for that galaxy.

2.1 Data Reduction

2.1.1 Bias Subtraction

The bias level is introduced onto the CCD chip for ensuring that the chip is working in a linear regime, after taking the image we have to subtract that introduced level. For the subtraction, during the observations night, a series of images have been taken with zero exposure. We have combined these images by averaging in IRAF (Image Reduction and Analysis Facility) [2] and we have checked that the bias is completely flat. It is, inside the uncertainties, the same value in all the image. Once we have checked this, we haven't used that combined bias to subtract it from all our images because we don't want to add the "noise" of the bias to the "noise" that is present in our images by default. Instead of that,

we have considered the overscan (part of the CCD that is not exposed to the light) of each one of the images to subtract the bias.

As we can see in Figure 2.1, each image has zone of overscan in two of the borders of the image. As the bias should be flat (and effectively it is) if we obtain the mean value of the counts for each pixel in the overscan area for both borders, the value should be the same if the bias does not have any gradient, in our case we only have a difference of 3 or 4 counts (which is a just 0.33 % the value of the bias level), so we can be sure that they are the same. For the bias subtraction, we have made a mean of the counts in both regions of the overscan and we have subtracted that constant number from each image with IRAF. Note that the value of the mean of the counts in the overscan area may not to be the same in all the images, so we will have different numbers for different images although those numbers have to be similar. With this, we are avoiding to add the noise of the bias image to the noise present in our images.

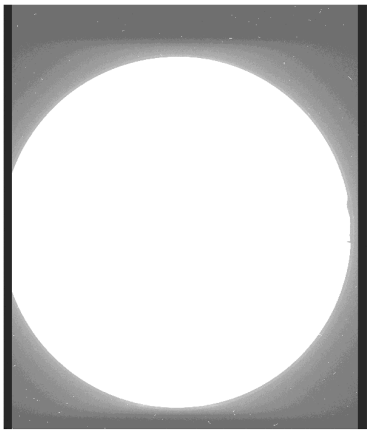

Figure 2.1: *Example of a saturated image, taken with ACAM, where we can see the overscan in both sides.*

2.1.2 Flat-Field Correction

Images were taken with a flat lighting on all the observation nights for each observed filter. Flat lighting was obtained by making sky flats at nightfall. Due to this, some images of the flats show stars distributed throughout the field. Most of these stars disappear when we combine the flats using IRAF and using the median of the data for the combination, but there have been certain images for some filters (Hα) where the stars have not been completely eliminated. In these cases we have used a GAIA [1] tool that allows us to adjust a given polynomial to the region we wanted from an image.

We have made this adjustment for the images that had bigger stars. As we can see in the following image (Figure 2.2), for the smaller stars, the adjustment works well, but for the larger stars the adjustment is not so good. Luckily, the stars in the flat are out of our field of study, so they do not present problems when using the flats to correct our images. We have made the polynomial adjustment just to obtain a visually cleaner image, although it does not affect the data. With all the flats of each filter combined, we have used them to divide each image of each filter by the corresponding flat and thus correct the defects of the pixel image sensitivity.

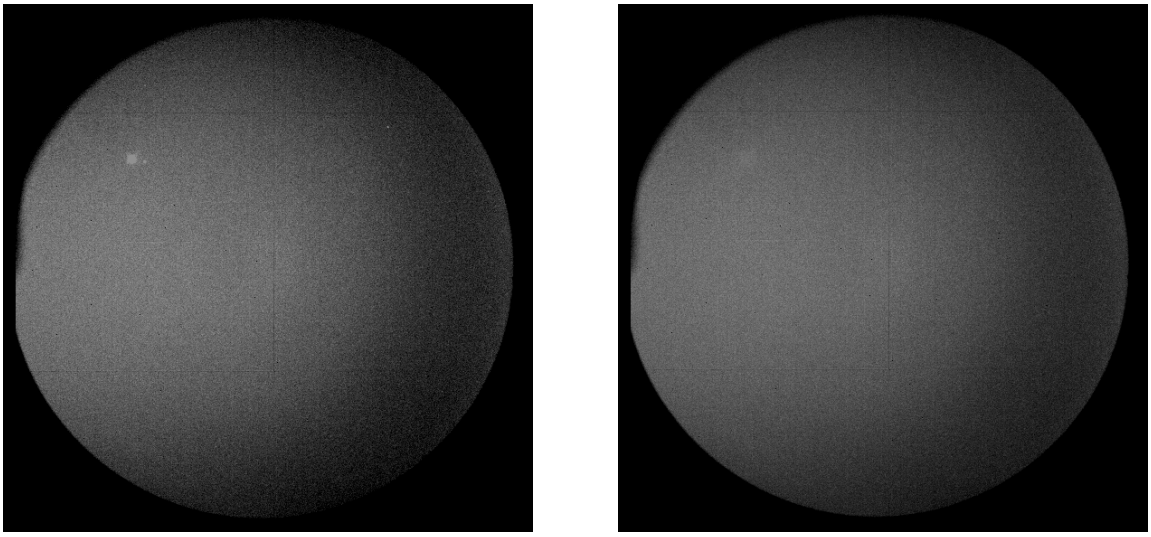

(a) Before the polynomial fit.

(b) After the polynomial fit.

Figure 2.2: *Comparison of the flat for the filter T4550 before and after the polynomial fit with GAIA [1].*

2.1.3 Combination, Smoothing and Alignment

Once we have all the images for each filter corrected of bias and flat, we proceed with the alignment and the combination of all the images for the same filter. Before the combination, we have to align all the images, to do that, we select in all the images three stars that are present in the field and that are common to all and them. Then, with IRAF, we know the positions of these stars of reference in all the images and we move the images to get all the stars in the same position. With that, we have aligned the images of one filter, we do the same with all the filters and then we start with the combination.

For the combination, as we can see in Table 2.2, we have different number of images with a different exposure time. In order to compare all this images we need that they have all the same integrated time, to do that, we divide each image by their exposure time in seconds so all the pixels in the images have dimension of counts per second. Once we do that, we proceed with the combinations of all the images of one filter. This combination is done to optimized the signal to noise ratio. Due to the noise is completely aleatory and the flux for a given source it is not, if we combined different images of the same source we will reduce the noise, and the signal to noise ratio will increase in a proportion similar to the root square of the number of images combined. We used a median combination and a parameter of rejection, the cosmic ray reject. We did that because our images present cosmic rays due to the high exposure time. The median combination use the median value in a pixel, so the higher values and the lower wont affect the value of that pixel and the cosmic ray reject wont use that values that are too high comparing with the standard deviation. With that we eliminate all the cosmic rays and we obtain a good and clear images of the galaxy for

each filter.

After the combination, we obtain four different images, one for each filter. Because the images were taken in different hours and days, all of them have different seeing that produce a different apparent size for the same source. As we want to compare the images we need that they have the same seeing in all of them. To do that, we measured the seeing for each filter that we can see in Table 2.3.

Filter	**Src. 1**	**Src. 2**	**Src. 3**	**Src. 4**	**Src. 5**	**Src. 6**	**Src. 7**	**Mean Seeing (pixels)**
T4550	4.22	4.37	4.33	4.19	4.12	4.22	4.10	4.22
T4880	4.75	4.50	4.69	4.48	4.30	4.39	4.27	4.48
T6590	7.02	6.65	7.08	6.48	6.39	6.54	6.67	6.69
T6770	7.22	7.24	7.18	7.29	7.18	7.20	7.08	7.20

Table 2.3: *Seeing in pixels for all the filters of different sources in M74.*

Note that the units of the seeing in Table 2.3 are in pixels but if we want to know the seeing in *arcsec* we just need to multiply all the values by 0.25, which is the pixel scale of ACAM. To compare the images, we have to convert the seeing of the better images to the worst seeing (which it the image for the Hα continuum). To do that, we use a Gaussian smooth function with IRAF, the idea of Gaussian smoothing is to use this 2-D distribution as a "point-spread" function, and this is achieved by convolution. After the smoothing, we have all the filters with the same seeing but know this images are not aligned, because we aligned the images for the same filter but the pointing of the telescope for different filters can change, so we do the same as we commented before and align the four images. After this process, we have all the images ready to the next step.

2.1.4 Continuum Subtraction

The reason why we need to observe in four filters and not only in Hα and Hβ is because, to get an image of any of these two emission lines, the filters used have a certain width, so we are not only observing in Hα or Hβ but also we are receiving flux from the galaxy's continuum. To correct this effect in the received flux, it is observed in another filter close to the filter that we want to correct from the galaxy's continuum but that does not include the emission line that we are interested in.

For the Hα and Hβ lines (T4880 and T6590), we use the other two images where the galaxy continuum appears (T4550 and T6770) always using the image of the continuum closest to the line in question to correct it. The method consists, basically, in subtracting

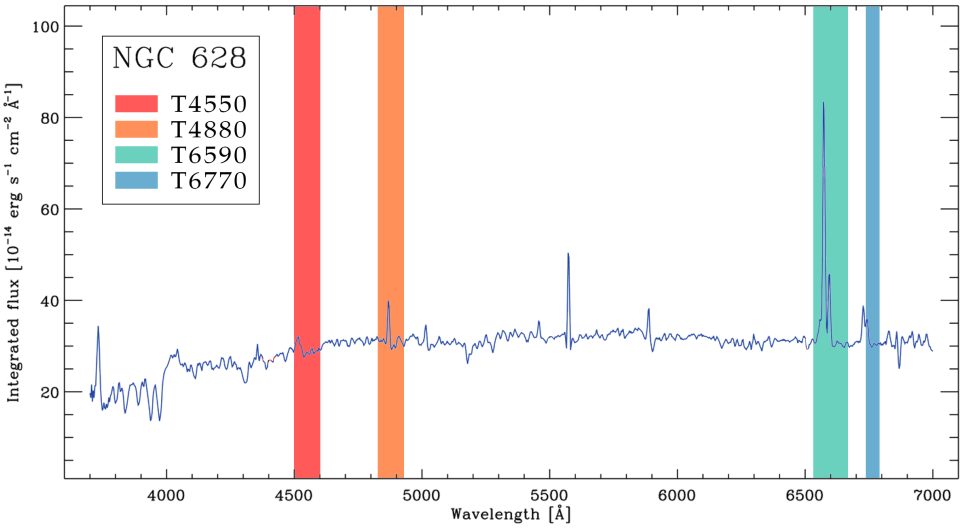

Figure 2.3: *Galaxy M74 spectrum, Sánchez et al. (2010) [25] with the position of the 4 filters used in this work.*

from the image of Hα or Hβ its image associated with the nearest galaxy continuum scaled by a certain factor.

Looking at Table 2.2, each filter has a different width and transmission, so the scale factor should be, in principle, different for each one. We have obtained this scale factor in a manual way, that is, we have multiplied by a different number for each filter of the continuum (T4550 or T6770), looking if that number should be bigger or smaller than one with the help of Table 2.2 and then, we have subtracted this image with IRAF to the image of the emission lines. After this, we verify that the galaxy's continuum does not appear in the resulting image, only the emission in Hα or Hβ of the galaxy. To know that, after the continuum subtraction we look the result image and check if the galaxy nucleus doesn't appears on it and the spiral arms doesn't appears neither, we look for the best scale factor that doesn't produce a darkened in the spiral arms (which means that we are subtracting too much) and that doesn't have a nucleos too bright (which means that we are not subtracting enough). The scale factor obtained for the Hα continuum is 2.85 and for Hβ it is 1.45.

2.1.5 Flux Calibration

After the basic reduction process, we have to calibrate the Hα and Hβ to have an appropriated units for the flux. Following Knapen et al. (1992) and Sánchez-Gallego et al. (2012) [24], the appropriate way of do a photometric calibration of the images would be if we consider the flux density f_λ as:

$$\log(f_\lambda) = -0.4\ \mathrm{mag}_\lambda - 8.42\ , \tag{2.1}$$

where f_λ is given in units of [erg s^{-1} cm^{-2} Å^{-1}]. Using the images that were taken in the nights of the observations to a know standard stars, these stars have the value of mag$_\lambda$ tabulated every few Å, so we can compare our flux for that stars with the tabulated flux and obtain the zero point factor as:

$$ZP = \frac{\Delta\lambda f_\lambda}{\chi} \qquad \left[\frac{\text{erg}}{\text{cm}^2 \text{ counts}}\right], \tag{2.2}$$

where χ represent the total flux of the standard star in units of [count s^{-1}]. So the flux for a certain region in our images would be:

$$\log(F) = ZP + \log(\text{counts}) \qquad \left[\frac{\text{erg}}{\text{cm}^2 \text{ counts}}\right]. \tag{2.3}$$

Although this method is the most adequate to perform the calibration of our data, due to a problem with the calibration images, we could not carry out this process so, in the next section, we will explain the method used by us for the calibration.

Cross Calibration

Due to a problem with the calibration images and the resulting impossibility of performing the calibration discussed above, we decided to cross-calibrate using the bibliography data for Hα and Hβ fluxes.

We compared our data with the data of the paper Sanchez et al. 2010) [25], their data were taken with spectroscopy and not with imaging but it is possible to cross calibrate with it. The images in the paper are calibrated in flux and their units are 10^{-16} erg s^{-1} cm^{-2} arcsec^{-2}. Besides, we have to take into account that their images have much less resolution than ours. We can know that because our pixel scale from ACAM is 0.25 arcsec/pixel and their is 2 arcsec/pixel.

To be able to compare our images of Hα and Hβ with Sanchez et al. 's images we need that they have the same resolution. To do that, we have made a Python [3] program taking into account that to have both images with the same pixel size (both pixels include the same area in the sky) we have to combine 64 pixels (8 x 8 pixels) in only one in our image. This process is know as hanning smoothing, for this smoothing we have do the sum of all the 64 pixels and put that value in that pixel.

Once we have all images in the same resolution (in all the images 1 pixel is equivalent to 4 arcsec^2) we can compare the fluxes for different Hα and Hβ regions to obtain the scale factor that will calibrate in flux our images. With this in mind, we have selected in Sanchez's images and in our, the same number of regions in order to compare between them. We have integrated the flux inside each one of this region and we obtain for each regions the values present in Table 2.4.

Region	**Our Hα Flux (counts/pixel)**	**Sanchez et al. Hα Flux (10^{-16} erg s^{-1} cm^{-2} pixel^{-1})**	**Our Hβ Flux (counts/pixel)**	**Sanchez et al. Hβ Flux (10^{-16} erg s^{-1} cm^{-2} pixel^{-1})**
R1	233.1	861.5	37.9	438.3
R2	516.0	1784.0	180.17	1302.8
R3	2793.5	5014.4	8.5	63.3
R4	477.4	337.4	33.8	438.4
R5	1053.2	1752.6	31.5	341.0
R6	1019.0	1018.4	96.8	604.0
R7	1450.5	1483.0	96.1	890.3
R8	3111.9	3228.7	120.2	1339.0
R9	1826.8	2441.7	118.5	1024.7
R10	2241.9	3120.1	55.5	528.7
R11	3300.3	5473.7	14.1	355.4
R12	824.3	1330.6	68.8	541.4
R13	2469.4	4261.6	48.9	202.4
R14	1348.0	1836.2	-	-
R15	1968.4	2792.8	-	-
R16	1528.5	2121.9	-	-
R17	1066.8	1085.9	-	-
R18	465.9	278.4	-	-
R19	542.9	708.0	-	-

Table 2.4: *Flux for the different regions in our images of Hα and Hβ and in Sanchez's images*

We have use fewer regions for Hβ than for Hα because our Hβ has a less signal-to-noise ratio and we have decided to choose just that regions which are the most brighter. The name of the regions doesn't correspond with the same region in both images. A closer view of the regions are added in Appendix A.

To obtain the scale coefficient, we have adjusted a line using a least square fit of the type $y = mx + n$ where y is the flux value for a region in the Sanchez et al.'s image, m is the slope of the straight line (which will be our scale factor), x is flux value for the same region but in our image and n is the intercept, that has to be equal or close to zero because when in Sanchez et al.'s image there is not flux, in our image we don't have to have flux neither. We used an linear fit because our CCD has an linear behavior, so the number of counts in any pixel has to be linearly proportional to the received flux on that pixel. Figure 2.4 represents this data adjustment.

We will obtain the error in the slope for the flux calibration taking into account the standard deviation of the data in both adjustments. We can calculate that error knowing that the standard deviation of the fit is the square root of the variance, so we have:

$$\sigma = \sqrt{\frac{1}{n}\sum_{i=1}^{n}(x_i - \bar{x})^2}\ , \tag{2.4}$$

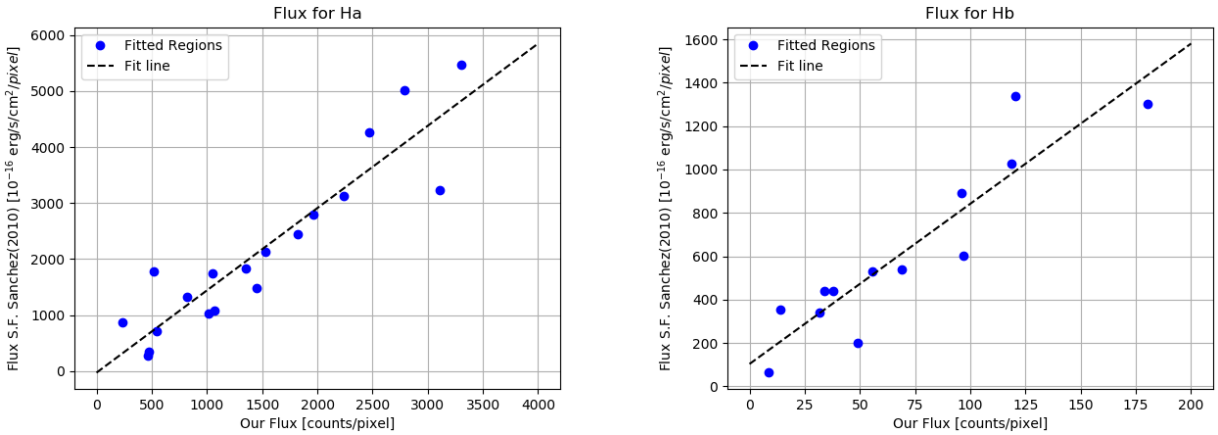

Figure 2.4: *Fit of the fluxes for the regions of the Hα (left) and Hβ (right) image.*

where n is the number of regions in the images, x_i is the flux of the region i in our image and $\bar{x}$ is the mean value of the flux for all regions in our images.

With that, the values of the fit for Hα and Hβ with its errors are:

$$\text{For H}\alpha \rightarrow \text{y} = (1.5 \pm 0.2)\text{x} + (-30 \pm 261) \tag{2.5}$$

$$\text{For H}\beta \rightarrow \text{y} = (7.4 \pm 0.9)\text{x} + (103 \pm 82) \tag{2.6}$$

Where, as we have said before, our scale factor, which we will have to multiply our Hα and Hβ images to have them calibrated, is the slopes of each lines. The correlation coefficient for the Hα fit is 0.92 and for Hβ fit is 0.92.

2.2 Final Images

We present here the final maps (not corrected for extinction) but scaled and in appropriated units.

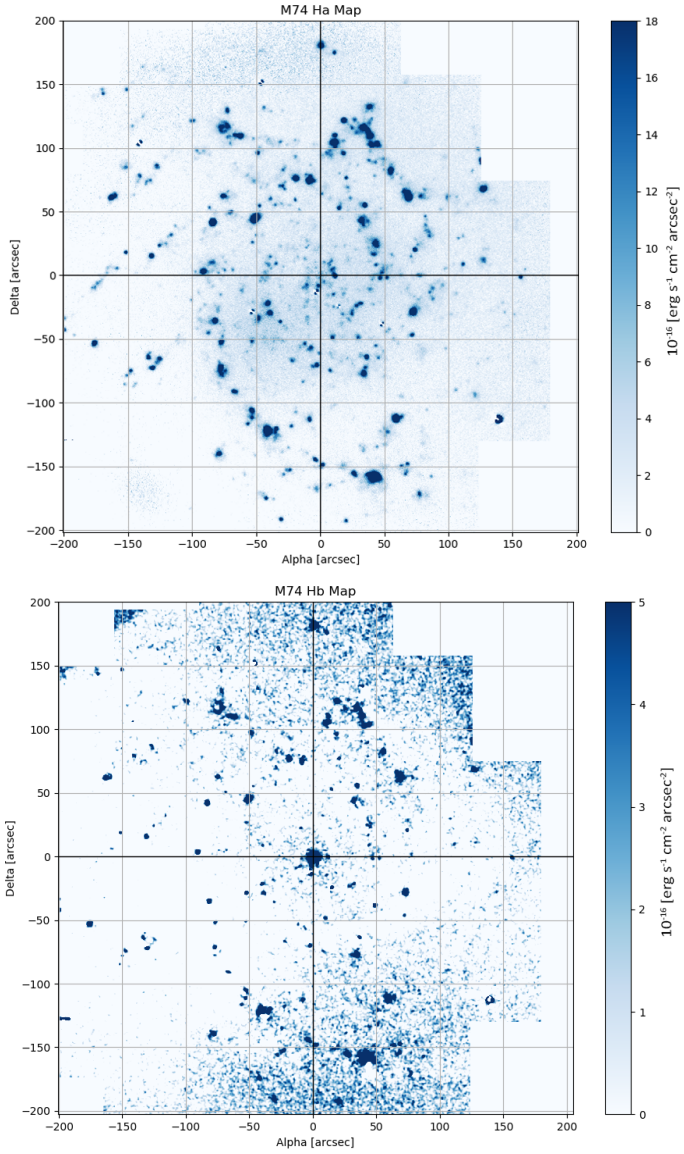

Figure 2.5: *Final Hα (top) and Hβ (down) flux maps.*

To have our finals images in physical units, we just need to remember that 1 pixel in our images is equivalent to 0.0625 arcsec^2 (0.25x0.25) so multiplying our images for the scale factor and dividing every pixel by 0.0625 we obtain the flux for Hα and Hβ in units of [erg s^{-1} cm^{-2} arcsec^{-2}]. The units of the map in Figure 2.5 are in 10^{-16} [erg s^{-1} cm^{-2} arcsec^{-2}].

CHAPTER 3

Theoretical Methodology

3.1 Received Intensity

We have seen, as introduction, a qualitative description of the extinction produced mainly by dust of the light that comes from a galaxy. In this chapter we will analyze, in a quantitative way, the effect on the extinction of light.

The relationship between the intensity of light emitted by a star and the intensity received from our observation point after passing through any material (in our case, interstellar dust and gas) is given by the radiative transport equation:

$$\frac{dI(\nu)}{dl} = -\kappa_\nu I(\nu) + j_\nu \ , \tag{3.1}$$

where $I(\nu)$ is the intensity of light emitted by the star at a given frequency in units of [erg cm^{-2} s^{-1} Hz^{-1} str^{-1}], dl is related to the length of the dust layer that the light has to go through, κ_ν is the absorption coefficient in units of [cm^{-1}] and j_ν is the emission coefficient of the medium in units of [erg cm^{-3} s^{-1} Hz^{-1} str^{-1}].

The dust emits radiation at infrared frequencies but since we will not use these frequencies for this work we can consider that, in the study frequencies, the dust does not emit radiation and the radiation is not scattered into the line of sight, so we can eliminate the emission coefficient from the expression ($j_\nu = 0$), and:

$$\frac{dI(\nu)}{dl} = -\kappa_\nu I(\nu) \ . \tag{3.2}$$

Solving that equation we have:

$$\frac{dI(\nu)}{I(\nu)} = -\kappa_\nu dl \rightarrow I(\nu) = I_0(\nu) e^{-\int_0^l \kappa_\nu dl} \ . \tag{3.3}$$

Defining the concept of optical depth as the integral of the absorption coefficient, we have:

$$\tau_\nu = \int_0^l \kappa_\nu dl \ , \tag{3.4}$$

and finally, we obtain the relationship between the intensity emitted and received based on the absorption coefficient as:

$$I(\nu) = I_0(\nu) e^{-\tau_\nu} \ . \tag{3.5}$$

For our convenience, we can change between frequency and wavelength knowing that $I(\nu)d\nu = I(\lambda)d\lambda$. So we obtain, in terms of wavelength, this expression:

$$I(\lambda) = I_0(\lambda) e^{-\tau_\lambda} \ . \tag{3.6}$$

3.2 Extinction

We define the extinction of any celestial object as the difference between the magnitude observed and emitted by that body:

$$A_\lambda = m_\lambda - m_{\lambda 0} = -2.5 \ \log\left(\frac{I(\lambda)}{I_0(\lambda)}\right) \ , \tag{3.7}$$

where A_λ represents the extinction coefficient and m the apparent magnitude of the object in a known filter. Taking into account expression 3.6, we can obtain:

$$A_\lambda = -2.5 \ \log\left(e^{-\tau_\lambda}\right) = 2.5 \ \log(e) \ \tau_\lambda \ . \tag{3.8}$$

We can relate the extinction and the colour excess through the equation:

$$A_\lambda = k(\lambda) E(B-V) \ , \tag{3.9}$$

where $k(\lambda)$ corresponds with an extinction law (attenuation curve) that we will see later and $E(B-V)$ is the colour excess of the filters B and V ($E(B-V) = A_B - A_V$).

Using expression 3.12, we can calculate the difference in the extinction at two different wavelengths as:

$$A_\lambda - A_{\lambda'} = (k(\lambda) - k(\lambda')) \ E(B-V) \ , \tag{3.10}$$

and using relation 3.8, we have:

$$2.5 \ \log(e)\tau_\lambda - 2.5 \ \log(e)\tau_{\lambda'} = (k(\lambda) - k(\lambda')) \ E(B-V) \ . \tag{3.11}$$

So the relation between the colour excess and the optical depth for two different wavelengths is:

$$E(B-V) = \frac{2.5 \ \log(e)}{(k(\lambda) - k(\lambda'))}(\tau_\lambda - \tau_{\lambda'}) \ . \tag{3.12}$$

The difference between two optical depths can be obtained from the emission lines of a galaxy. This difference can be extracted if we use expression 3.6 for the intensity. That expression can be normalized for any different wavelength, if we do that we obtain:

$$\frac{I(\lambda)}{I(\lambda')} = \frac{I_0(\lambda)}{I_0(\lambda')} e^{-(\tau_\lambda - \tau_{\lambda'})} \, . \tag{3.13}$$

In this point, as we have seen in Chapter 2, we will use the Hα and Hβ images. This is done just because we can obtain a better signal to noise ratio in this images, so we can know better the extinction using this filters and we can compare our flux in those filters with the Balmer decrement. The previous expression is transformed into:

$$\frac{I(H_\alpha)}{I(H_\beta)} = \frac{I_0(H_\alpha)}{I_0(H_\beta)} e^{-(\tau_{H_\alpha} - \tau_{H_\beta})} \, , \tag{3.14}$$

so using that filters and operating the equation, we have that the difference in the optical depth is:

$$(\tau_{H_\alpha} - \tau_{H_\beta}) = -\ln\left(\frac{I(H_\alpha)/I(H_\beta)}{I_0(H_\alpha)/I_0(H_\beta)}\right) \, . \tag{3.15}$$

Replacing this in expression 3.12 we have:

$$E(B-V) = \frac{2.5 \ \log(e)}{(k(H_\beta) - k(H_\alpha))} \ln\left(\frac{I(H_\alpha)/I(H_\beta)}{I_0(H_\alpha)/I_0 \ .(H_\beta)}\right) \tag{3.16}$$

Converting the previous expression to a decimal logarithm, we finally get the expression for the colour excess:

$$E(B-V) = \frac{2.5}{(k(H_\beta) - k(H_\alpha))} \log_{10}\left(\frac{I(H_\alpha)/I(H_\beta)}{I_0(H_\alpha)/I_0(H_\beta)}\right) \, . \tag{3.17}$$

Where $k(H_\beta)$ and $k(H_\alpha)$ can be obtained using an extinction law that we will comment later and the quotient $I_0(H_\alpha)/I_0(H_\beta)$ is the ratio of this two emission lines (the Balmer decrement), following Osterbrock 1975 [23] and considering a case B recombination and an electron temperature of 10.000 K, that ratio should be 2.86.

We can relate the colour excess to the extinction using the ratio of total-to-selective extinction. This ratio compares the extinction and reddening properties of grains and it is sensitive only to the grain composition, size and shape:

$$R_V = \frac{A_V}{E(B-V)} \rightarrow A_V = R_V E(B-V) \, . \tag{3.18}$$

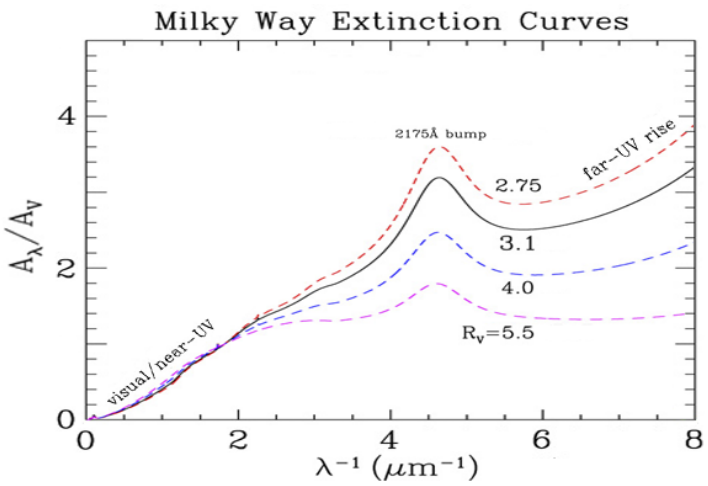

Figure 3.1: *Interstellar extinction curves of the Milky Way (RV = 2.75, 3.1, 4.0, 5.5)[22].*

The ratio of total to selective extinction (R_V), is affected by the grain size. Particles in the galaxy that have size much longer than the wavelength of light produce gray extinction, this extinction is the same for all wavelengths. On other hand, small particles produce Rayleigh scattering, in this case, the extinction is inversely proportional to the wavelength ($\alpha\ \lambda^{-4}$). This difference in grains produces differences in the extinction curves, as we can see in Figure 3.1. Large R_V extinction curves (for example $R_V = 5.5$ in the Orion region) have a grain size distribution that is weighted to larger sizes or is deficient in smaller grains. A smaller R_V is related to smaller grain size. For the standard extinction curve, typical of the diffuse interstellar medium $R_V = 3.1$. This is the typical value for galaxies, and for our calculations we will use that value.

3.2.1 Extinction Law

The most used attenuation curve for galaxies is the law derived by Calzetti et al. (2000) [5]. They derived a law as a purely empirical result from a sample of nearby starburst galaxies between 0.12 μm and 2.2 μm. Later, Fischera et al. (2003) [10] demonstrated that the theoretical attenuation of light through a turbulent dusty foreground medium can provide an excellent fit to the empirical Calzetti attenuation curve so they contributed by giving a more physical explanation for the attenuation curve.

The attenuation curve is modeled by this expression:

$$k(\lambda) = \begin{cases} 2.659\left(-2.156 + \frac{1.509}{\lambda} - \frac{0.198}{\lambda^2} + \frac{0.011}{\lambda^3}\right) + R_V & 0.12\ \mu m \leq \lambda \leq 0.63\ \mu m \\ 2.659\left(-1.857 + \frac{1.040}{\lambda}\right) + R_V & 0.63\ \mu m \leq \lambda \leq 2.20\ \mu m \end{cases}, \quad (3.19)$$

which is the expression that we will use in our calculations to obtain the extinction map. In our case, we have Hα and Hβ lines, so following the extinction law we have a value of

$k(H_\alpha) = 2.3758$ and $k(H_\beta) = 3.6481$ for that filters.

3.3 Flux Correction

Once we have calculated the extinction in the galaxies we can correct the flux for a given wavelength to obtain the real flux emitted for any region in a galaxy. In order to do that we only need to know that the intrinsic flux is related with the extinction coefficient by the formula:

$$F_0(\lambda) = F(\lambda)10^{0.4A_\lambda} \ , \tag{3.20}$$

where $F_0(\lambda)$ is the emitted flux by line of sight of the galaxy in a given wavelength and $F(\lambda)$ is the received flux for the same line of sight in the same wavelength. Using equation 3.12 we can calculate the emitted flux as:

$$F_0(\lambda) = F(\lambda)10^{0.4k(\lambda)E(B-V)} \ , \tag{3.21}$$

where $k(\lambda)$ is given by expression 3.19 and $E(B-V)$ by equation 3.17.

3.4 Star Formation Rate

The derivation of the SFR relies on conversion factors depending on the indicator used. The fundamental equation to link the intrinsic luminosity emitted by stars at wavelength λ and a time t is (Buat [4]):

$$\mathrm{L}(\lambda, t) = \int_0^t \int_{M_{\mathrm{low}}}^{M_{\mathrm{up}}} F_\lambda(m, \theta)\ \mathrm{SFR}(t-\theta)\ \psi(m)\mathrm{dm}\ \mathrm{d}\theta \ , \tag{3.22}$$

where $F_\lambda(m, \theta)$ are an evolutionary stellar tracks, ψ is the initial mass function and $SFR(t-\theta)$ is the star formation rate function. Assuming a constant SFR over a timescale T, the SFR becomes simply proportional to the luminosity integrated over T. The timescale is chosen in order that the luminosity at a given wavelength reaches a steady state:

$$\mathrm{SFR} = \left(\int_0^t \int_{M_{\mathrm{low}}}^{M_{\mathrm{up}}} F_\lambda(m, \theta)\ \mathrm{SFR}(t-\theta)\ \psi(m)\mathrm{dm}\ \mathrm{d}\theta \right)^{-1} \cdot \mathrm{L}(\lambda) \ . \tag{3.23}$$

The value of the conversion factor SFR=$C \cdot \mathrm{L}(\lambda)$ is calculated with a spectral synthesis model. This models are calculated using a grid of stellar evolution tracks that are converted into a spectrum using stellar atmosphere models. The individual stellar templates are then summed together, weighted by an initial mass function, to synthesize the luminosities, colours, or spectra of single-age populations as functions of age. These isochrones can then be added in linear combination to synthesize the spectrum or colours of a galaxy with an arbitrary star formation history.

Using recombination lines to measure the flux, as we are doing in this work, provide a direct sensitive probe of the young massive stellar population. Only stars with masses $> 10M_{\odot}$ and lifetimes < 20 Myr contribute significantly to the integrated ionizing flux, so the emission lines provide a nearly instantaneous measure of the SFR, independent of the previous star formation history. Using the calibrations of Kennicutt et al. (1994) [18] we can obtain the star formation rate using the expression:

$$\mathrm{SFR} = 7.9 \cdot 10^{-42} \mathrm{L}(\mathrm{H}\alpha) \ , \tag{3.24}$$

were the star formation rate is measure in $M_{\odot}$/year and the luminosity in units of erg/s.

CHAPTER 4

Results and Discussion

4.1 Extinction Map

The emission lines ratios can give information about the physical properties of the emitting gas. The advantage of obtain an emission map, instead of just one spectrum of the galaxy, is that we can measure the physical properties point to point of the galaxy that we are interested in so we can study smaller structures inside it and get a better know of the processes that are occurring.

Using the described observations in Chapter 3, we can obtain the dust extinction distribution in our studied galaxy (Figure 4.1). This dust distribution is represented in terms of the visual extinction A_V, measured in magnitudes, using for that the emission lines ratio Hα/Hβ, as we commented in Chapter 3. We have only considered those regions where the Hα and Hβ emission was greater than three times the standard deviation (3σ) of the background of this images. This selection produce that we only take into account the parts of the galaxy where there are a greater flux of Hα and Hβ. Due to the form of the expression for the extinction coefficient (A_V), those pixels were the quotient between the Hα and Hβ fluxes were smaller than the tabulated quotient between this lines, which is 2.86 (Osterbrock 2005 [23]) are not taking into account because negative extinction have no sense. In theory, in the regions were there is extinction, this quotient will never be smaller than 2.86 because the extinction will always be greater for Hβ than for Hα, in other words, the extinction is always bigger for smaller wavelengths. But, due to the sensitivity of our data, this happens in our extinction map.

The mean extinction, considering all the values bigger than zero that appear in the extinction map is:

$$A_V = 0.98 \pm 0.62 \quad [\text{mag}] \, . \tag{4.1}$$

Where the uncertainties in the extinction is obtained taking into account that we only have error in the obtaining of the flux for the Hα and Hβ maps (explained in Chapter 2). The errors on this maps are explain in Section 4.2.

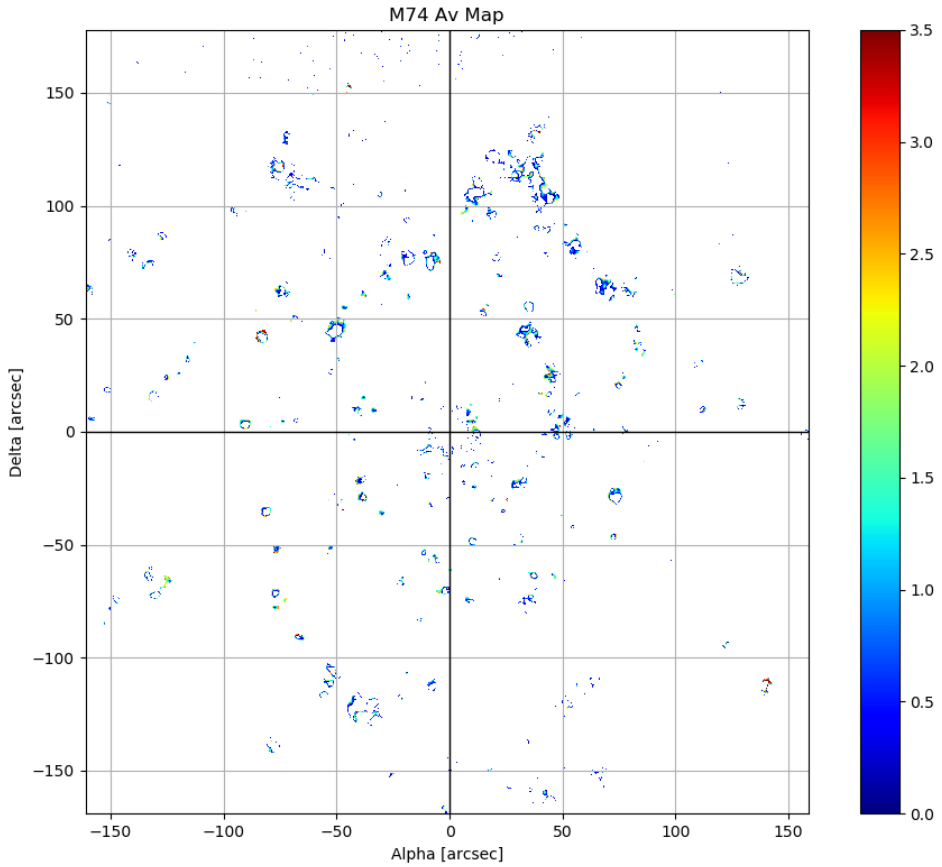

Figure 4.1: *Dust attenuation map (A_V) measured in magnitudes.*

Using error propagation in the expression for the calculation of the extinction map (Chapter 3), we have:

$$A_V = K\ \log_{10}\left(\frac{F_{H_\alpha}/F_{H_\beta}}{C}\right) = K\ \log_{10}\left(\frac{F_{H_\alpha}}{F_{H_\beta}}\right) - K\ \log_{10}(C)\ , \tag{4.2}$$

where K and C are constant that can be seeing in the expression 3.17 and 3.18. F_{H_β} and F_{H_α} are the scaled fluxes. Using error propagation on that expression:

$$\Delta A_V = \left|\frac{\delta A_v}{\delta F_{H_\alpha}}\right| \Delta F_{H_\alpha} + \left|\frac{\delta A_V}{\delta F_{H_\beta}}\right| \Delta F_{H_\beta}\ , \tag{4.3}$$

where ΔF_{H_α} and ΔF_{H_β} are given by the expression 4.7. Using that and doing the derivative we obtain that the error for each pixel in the extinction map is:

$$\Delta A_V = \left(\frac{K}{F_{H_\alpha}\ln(10)}\right) f_{H_\alpha} \Delta \mathrm{SF}_{H_\alpha} + \left(\frac{K}{F_{H_\beta}\ln(10)}\right) f_{H_\beta} \Delta \mathrm{SF}_{H_\beta}\ . \tag{4.4}$$

Using the expression for the scaled flux $F_{H_\lambda} = \mathrm{SF} \cdot f_{H_\lambda}$, where λ means that the expression is valid for both lines, we can relate the error in the extinction coefficient with the relation between the scale factor and its error with the expression:

$$\Delta A_V = \frac{K}{\ln(10)} \left(\frac{\Delta \mathrm{SF}_{H_\alpha}}{\mathrm{SF}_{H_\alpha}} + \frac{\Delta \mathrm{SF}_{H_\beta}}{\mathrm{SF}_{H_\beta}} \right) . \tag{4.5}$$

As the mean of A_V is $\bar{A_V} = \sum_i^n \frac{A_{V_i}}{n}$ where A_{V_i} is the A_V value for one pixel of the image and n is the total number of pixels considered in the mean. The error in the mean will be:

$$\Delta \bar{A_V} = \frac{\delta \bar{A_V}}{\delta A_{V_i}} \Delta A_{V_i} = \frac{1}{n} \left(\sum_i \Delta A_{V_i} \right) . \tag{4.6}$$

So the error in the mean of the A_V value will be the mean of the errors in each pixel taken into account to calculate the mean A_V value. But as we can see in the expression 4.5, due to our consideration that we take the error in the determination of the flux as the error in the scale factor, our error of A_v for each pixel only depend of the error in the scale factor (which is a constant for all the pixels) so the error in the extinction will be a constant as well.

As we can see, our extinction map has not got much information in many parts of the galaxy and this is mainly due to our Hβ map. That map has a low signal to noise ratio and it just show small regions where the Hβ flux is higher. The problem with the Hβ map it is caused by the scattered moonlight in the continuum images for that filter. That light produce a continuum excess in parts of the image so we can't subtract the continuum properly. If we add to that the flux calibration, which is the best that we can do due to our problems with the calibration but is not the best for our purpose we obtain a map which not much information. The errors that we have for the extinction coefficient just depend of the error in the flux calibration. As we have big errors in that calibration we will obtain the same here. Looking to the mean value of the map it has sense, inside the error, but is not a reliable value. The few regions of the map that have a accepted value of Av are localized in the spiral arms of the galaxy, this looks logical because is there where the most part of the Hα and Hβ regions are localized.

4.2 Hα and Hβ Fluxes and Star Formation Rate

Using the expression 3.21, we can correct our maps for Hα and Hβ of the extinction but, due to our extinction map don't cover many parts of the galaxy it has no sense to correct the whole maps of the extinction, instead of that we will use HII regions to get a better idea of the galaxy fluxes.

The errors on the Hα and Hβ fluxes can be calculated knowing that we only have error in the scale factor (as we commented in Chapter 2). Considering that the error in the scale

factor its named as $\Delta \mathrm{SF}_{H_\alpha}$ or $\Delta \mathrm{SF}_{H_\beta}$ depending of the flux that we want to know, the error in each pixel of the images for the final flux can be calculated with:

$$\Delta F_{H_\alpha} = f_{H_\alpha} \Delta \mathrm{SF}_{H_\alpha} \quad and \quad \Delta F_{H_\beta} = f_{H_\beta} \Delta \mathrm{SF}_{H_\beta} \ . \tag{4.7}$$

The f_{H_α} and f_{H_α} are the fluxes for that lines that are not scaled by the scaled factor (SF) of Section 2.1.5.

We can see in the maps that our image for Hα is better than our Hβ because we can see more details and more regions on it. This is something logical because we received more flux form Hα so we have a better signal to noise ratio on that image. So our maps are limited by the worst image, which is Hβ. Parts of sky in the Hβ image have a high flux (the sky should be close to zero because it was subtracted from both images in the reduction process), this is cause probably by the moonlight and it is the main reason why we can get a detailed map for our extinction coefficient.

In order to obtain more information about our data, we decided to study different regions of the galaxy separately, with that we get more flux than just comparing the image pixel by pixel and we can get better values for the extinction and we can correct that regions from it. In Chapter A we can see the regions that we study separately in detail. We have choose that regions because they had a decent Hα and Hβ integrated fluxes, so we can study all the points that we want to do on that region. In the next table (Table 4.1) we can see a detailed study of individuals regions on the galaxy.

As we can clearly in Table 4.1, the same HII region have a much higher value for Hα than for Hβ so it has sense, as we explain before. Using the value for the extinction coefficient of each region we have corrected the fluxes as we can see in the table. The units of the fluxes are in 10^{-13} [erg s^{-1} cm^{-2}] for the corrected and the not corrected fluxes. Comparing our values for the Hα flux with the values obtained in other papers, we can see that we obtain the same value for the flux our region R14 than the flux of Ferguson et al. (1998) [9]. And comparing our value for the flux with the values of Kennicutt and Hodge (1980) [17] we can clearly see that all our values are comparable and have the same magnitude order than their values for the Hα flux.

For the extinction coefficient, we can see that the value of it vary from region to region, the mean A_V value of all the regions is 1.54 ± 0.62 [mag], this result is comparable with the A_V result obtained by Sánchez et al. (2010) [25]. Comparing our value with other paper that study separately regions in NGC628, Ferguson et al. (1998)[9] we have a low value in the extinction, but still comparable with the errors. Taking into account the distance of the regions from the centre of the galaxy, we can see that there is no apparent trend of the extinction along the spiral arms or in any radial direction.

We have used the flux for integrated regions of the galaxy to obtain the star formation rate in each region. To do that, we transformed the dust-corrected flux densities to absolute luminosities (L=$F_{H_\alpha} 4\pi d^2$), using the same distance to the galaxy described in Section 1.3. With that luminosities we obtain the value for the star formation rate, as we can see in Table 4.1. The star formation rate on that table was calculated following the same procedure explained in Chapter 3 using expression 3.24.

Table 4.1 shows the star formation rate for each region in units of $[M_\odot\ yr^{-1}]$. As expected, that regions that are close to the spirals arms have an stronger star formation that the others (that regions can be seen in detail in Appendix A). The positions of the regions in the galaxy can be seen in Figure 4.2. All the values for the SFR are in the same magnitude order than the values found in the literature. The total star formation rate of all the region is 0.9 $M_\odot\ yr^{-1}$ which is smaller than the values encountered in the bibliography (Sánchez et al. (2011)[25]) but is logical because we are not considering all the regions of the galaxy.

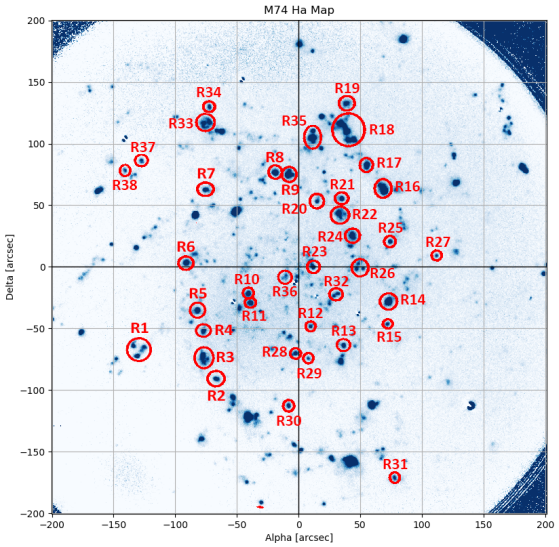

Figure 4.2: *Region's localization in the galaxy.*

Although we have just a few regions we have found that the start formation rate have a maximum close to 50 arcsec of distance to the galaxy centre (Figure 4.3). Converting that distance into kpc we found that at 2.35 kpc we have that maximum. This result is compatible with Gusev et al. (2015) [14], where they show the maximum in the same distance.

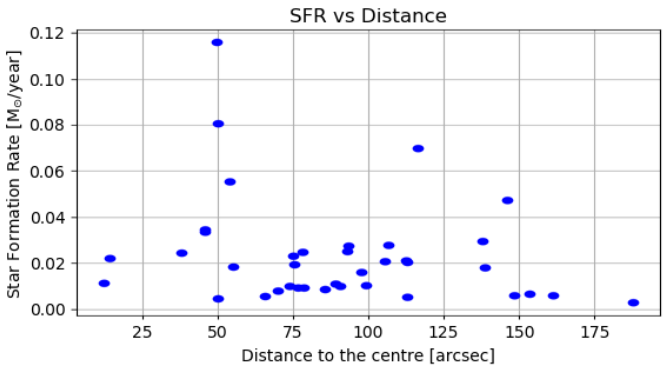

Figure 4.3: *Star formation rate vs distance to the centre of M74.*

Region	Alpha (arcsec)	Delta (arcsec)	Distance (arcsec)	Hα Received 10^{-13} (erg s^{-1} cm^{-2})	Hα Corrected 10^{-13} (erg s^{-1} cm^{-2})	Hβ Received 10^{-13} (erg s^{-1} cm^{-2})	Hβ Corrected 10^{-13} (erg s^{-1} cm^{-2})	Mean A_V (mag)	SFR $M_\odot$/year
R1	-129	-67	146.0	1.36 ± 0.13	4.62	0.24 ± 0.03	1.61	1.73 ± 0.62	0.047
R2	-66	-91	112.7	0.39 ± 0.04	1.99	0.05 ± 0.01	0.69	2.29 ± 0.62	0.021
R3	-77	-71	105.4	0.71 ± 0.07	2.04	0.14 ± 0.01	0.71	1.49 ± 0.62	0.021
R4	-77	-52	92.9	0.39 ± 0.04	2.45	0.05 ± 0.01	0.85	2.58 ± 0.62	0.025
R5	-81	-35	88.9	0.71 ± 0.07	1.08	0.19 ± 0.02	0.37	0.59 ± 0.62	0.011
R6	-90	3	90.5	0.74 ± 0.07	0.96	0.22 ± 0.02	0.33	0.38 ± 0.62	0.010
R7	-75	62	97.6	0.46 ± 0.04	1.56	0.08 ± 0.01	0.54	1.70 ± 0.62	0.016
R8	-19	76	78.3	0.85 ± 0.08	9.03	0.29 ± 0.03	0.31	0.08 ± 0.62	0.009
R9	-9	75	75.5	1.35 ± 0.13	1.91	0.39 ± 0.05	0.66	0.48 ± 0.62	0.020
R10	-40	-22	45.6	0.51 ± 0.05	3.38	0.06 ± 0.01	1.18	2.66 ± 0.62	0.035
R11	-36	-28	45.9	0.65 ± 0.06	3.27	0.09 ± 0.01	1.14	2.29 ± 0.62	0.034
R12	10	-49	50.0	0.23 ± 0.02	0.45	0.05 ± 0.01	0.15	0.92 ± 0.62	0.005
R13	37	-64	73.9	0.38 ± 0.03	0.97	0.08 ± 0.01	0.34	1.31 ± 0.62	0.010
R14	73	-28	78.1	1.78 ± 0.18	2.42	0.52 ± 0.06	0.84	0.44 ± 0.62	0.025
R15	72	-46	85.7	0.19 ± 0.02	0.82	0.03 ± 0.01	0.28	2.02 ± 0.62	0.009
R16	69	63	93.4	2.43 ± 0.24	2.68	0.80 ± 0.10	0.93	0.14 ± 0.62	0.028
R17	55	82	99.1	0.84 ± 0.08	0.99	0.26 ± 0.03	0.34	0.23 ± 0.62	0.010
R18	38	110	116.5	4.75 ± 0.48	6.84	1.36 ± 0.17	2.39	0.52 ± 0.62	0.070
R19	38	132	137.9	0.46 ± 0.04	2.88	0.06 ± 0.08	1.00	2.58 ± 0.62	0.030
R20	15	53	55.0	0.25 ± 0.02	1.80	0.03 ± 0.00	0.63	2.79 ± 0.62	0.019
R21	35	55	65.6	0.52 ± 0.05	0.53	0.18 ± 0.02	0.18	0.01 ± 0.62	0.006
R22	34	42	54.0	1.06 ± 0.10	5.40	0.15 ± 0.02	1.89	2.30 ± 0.62	0.055
R23	12	0	12.0	0.43 ± 0.04	1.08	0.09 ± 0.01	0.38	1.32 ± 0.62	0.011
R24	43	25	49.9	0.84 ± 0.08	7.87	0.08 ± 0.01	2.75	3.16 ± 0.62	0.081
R25	74	20	76.6	0.31 ± 0.03	0.91	0.06 ± 0.01	0.31	1.50 ± 0.62	0.009
R26	49	0	49.5	0.86 ± 0.08	1.33	0.07 ± 0.01	3.96	3.65 ± 0.62	0.116
R27	112	9	112.3	0.16 ± 0.01	2.04	0.01 ± 0.01	0.71	3.57 ± 0.62	0.021
R28	-2	-70	70.0	0.33 ± 0.03	0.76	0.07 ± 0.01	0.26	1.18 ± 0.62	0.008
R29	8	-74	74.9	0.14 ± 0.01	2.25	0.01 ± 0.01	0.78	3.93 ± 0.62	0.023
R30	-8	112	112.7	0.31 ± 0.03	0.52	0.08 ± 0.01	0.18	0.74 ± 0.62	0.005
R31	78	171	187.9	0.22 ± 0.02	0.26	0.07 ± 0.01	0.09	0.23 ± 0.62	0.003
R32	30	-22	37.9	0.45 ± 0.04	2.40	0.06 ± 0.01	0.84	2.37 ± 0.62	0.025
R33	-75	116	138.5	1.37 ± 0.13	1.76	0.41 ± 0.05	0.61	0.36 ± 0.62	0.018
R34	-72	129	148.1	0.28 ± 0.02	0.58	0.06 ± 0.01	0.20	1.00 ± 0.62	0.006
R35	11	106	106.5	2.27 ± 0.23	2.73	0.72 ± 0.09	0.95	0.26 ± 0.62	0.028
R36	-11	-8	14.0	0.29 ± 0.03	2.14	0.03 ± 0.01	0.75	2.80 ± 0.62	0.022
R37	-127	86	153.3	0.23 ± 0.02	0.65	0.04 ± 0.01	0.22	1.47 ± 0.62	0.007
R38	-141	78	161.1	0.16 ± 0.01	0.57	0.02 ± 0.01	0.20	1.78 ± 0.62	0.006

Table 4.1: *Hα and Hβ fluxes in 10^{-13} [erg s^{-1} cm^{-2}] for different regions of the galaxy before and after the extinction correction, its A_V value and the star formation rate for each region.*

CHAPTER 5

Conclusions

In this work we present Hα and Hβ images of the galaxy NGC 628 obtained by the William Herschel Telescope in La Palma. Problems in the data force us to do a cross calibration with other data in the bibliography. This calibration, and the low quality of the Hβ image, show the limitation of using these data to obtain an extinction map of this galaxy. Instead of using that map, several integrated regions of the galaxy were use to obtain the extinction, the star formation rate and the calibrated flux. With that data we can extract this conclusions as a summary of the work:

- The quality of the A_V map reside mainly in the good obtaining and reduction of the Hβ image.
- The mean A_V value for the map, and the mean A_V of all the selected regions of the galaxy are of 0.98 ± 0.62 and 1.54 ± 0.62 respectively. Both values are (inside the errors) comparable with the values in the literature.
- The star formation rate of all regions have values between 0.003 and 0.116 $[M_\odot\ yr^{-1}]$, in agreement with previous studies.
- The sum of the star formation rate for all the selected regions is of 0.9 $[M_\odot\ yr^{-1}]$ which is smaller than the star formation rate for all the galaxy.

Bibliography

[1] "GAIA is a derivative of the Skycat catalogue and image display tool, developed as part of the VLT project at ESO. Skycat and GAIA are free software under the terms of the GNU copyright. the 3D facilities in GAIA use the VTK library."

[2] "IRAF is distributed by the National Optical Astronomy Observatories, which are operated by the Association of Universities for Research in Astronomy, Inc., under cooperative agreement with the National Science Foundation."

[3] "Python Software Foundation. Python Language Reference, version 2.7. Available at http://www.python.org."

[4] V. Buat, "How to measure star formation rates in galaxies?" Aix-Marseille Université, CNRS, LAM (Laboratoire d'Astrophysique de Marseille) UMR7326, 13388, Marseille, Franc.

[5] D. Calzetti, L. Armus, R. C. Bohlin, A. L. Kinney, J. Koornneef, and T. Storchi-Bergmann, "The dust content and opacity of actively star-forming galaxies," *The Astrophysical Journal, Volume 533, Issue 2, pp. 682-695.*, 2000.

[6] J. A. Cardelli, G. C. Clayton, and J. S. Mathis, "The relationship between infrared, optical, and ultraviolet extinction," *The Astrophysical Journal, Part, 1 Vol. 345, Oct. 1, 1989, p. 245-256.*, 1989.

[7] Chandra X-Ray Observatory, "M74: X-rays signal presence of elusive intermediate-mass black hole," 2005.

[8] K. Fathi, J.E.Beckman, A. Zurita, M. Relaño, J. Knapen, O.Daigle, O. Hernandez, and C. Carignan, "Evolution of structure in late-type spiral galaxies. I. Ionized gas kinematics in NGC 628," *Astronomy and Astrophysics Volume 466, Number 3, May II 2007*, 2007.

[9] A. M. N. Ferguson, J. Gallagher, and R. F. Wyse, "The extreme outer regions of disk galaxies. I. Chemical abundances of HII regions." *The Astronomical Journal, Volume 116, Number 2*, 1998.

[10] J. Fischera, M. A. Dopita, and R. S.Sutherland, "Starburst galaxies: Why the calzetti dust extinction law?" *The Astrophysical Journal, 599:L21-L24,2003*, 2003.

[11] A. Garcia, "General study of group membership. II. Determination of nearby groups," *Astronomy & Astrophysics Supplement Series, vol. 100, no. 1, p. 47-90.*, 1993.

[12] R. D. Gehrz, "Sources of stardust in the galaxy," *International Astronomical Union. Symposium no. 135, Kluwer Academic Publishers*, 1989.

[13] K. D. Gordon, G. C. Clayton, K. A. Misselt, A. U. Landolt, and M. J. Wolff, "A quantitative comparison of the Small Magellanic Cloud, Large Magellanic Cloud, and Milky Way ultraviolet to near-infrared extinction curves," *The Astrophysical Journal, Volume 594, Number 1*, 2003.

[14] A. Gusev, F. Sakhibov, and Y. N. Efremov, "Star formation rates and the kinematics of gas in the spiral arms of NGC 628," *Astronomische Nachrichten, vol. 48, Issue 12, p.995-1004*, 2015.

[15] M. A. Hendry, S. J. Smartt, J. R. Maund, A. Pastorello, L. Zampieri, S. Benetti, M. Turatto, E. Cappellaro, W. P. S. Meikle, R. Kotak, M. J. Irwin, P. G. Jonker, L. Vermaas, R. F. Peletier, H. van Woerden, K. M. Exter, D. L. Pollacco, S. Leon, S. Verley, C. R. Benn, and G. Pignata., "A study of the Type II-P Supernova 2003gd in M74," *Monthly Notices of the Royal Astronomical Society, Volume 359, Issue 3, pp. 906-926.*, 2004.

[16] International Astronomical Union, "Definitions of terms in meteor astronomy," *Commission F1 of the International Astronomical Union*, 2017.

[17] R. Kennicutt and P. Hodge, "HII regions in NGC 628. III. Ha luminosities and the luminosity function," *The Astrophysical Journal, Part 1, vol. 241, p. 573-586.*, 1980.

[18] R. C. Kennicutt, P. Tamblyn, and C. W. Congdon, "Past and future star formation in disk galaxies," *The Astrophysical Journal, 435:22-36, 1994 November 1*, 1994.

[19] R. S. Klessen and S. C. O. Glover, *Physical Processes in the Interstellar Medium.* Cornell University Library, 2014.

[20] F. Koliopanos, "Intermediate mass black holes: A brief review," *Proceedings of Science*, 2018.

[21] J. Krelowski and J. Papaj, "The interestellar extinction curve," *Astronomical Society of the Pacific, vol. 105, no. 693, p. 1209-1221.*, 1993.

[22] A. Li, "The central engine of active galactic nuclei," *ASP Conference Series*, 2007.

[23] D. E. Osterbrock and G. J. Ferland, *Astrophysics of Gaseous Nebulae and Active Galactic Nuclei.* University Science Books, 2005.

[24] J. R. Sanchez-Gallego, J. H. Knapen, C. D. Wilson, P. Barmby, M. Azimlu, and S. Courteau, "The JCMT Nearby Galaxies Legacy Survey , VII. Ha imaging and massive star formation properties," *Monthly Notices of the Royal Astronomical Society, Volume 422, Issue 4, pp. 3208-3248.*, 2012.

[25] S. F. Sánchez, F. F. Rosales-Ortega, R. C. Kennicutt, B. D. Johnson, A. I. Diaz, A. Pasquali, and C. N. Hao, "PPAK Wide-field Integral Field Spectroscopy of NGC 628 – I. The largest spectroscopic mosaic on a single galaxy," *Monthly Notices of the Royal Astronomical Society, Volume 410, Issue 1, pp. 313-340.*, 2010.

APPENDIX A

FIGURES

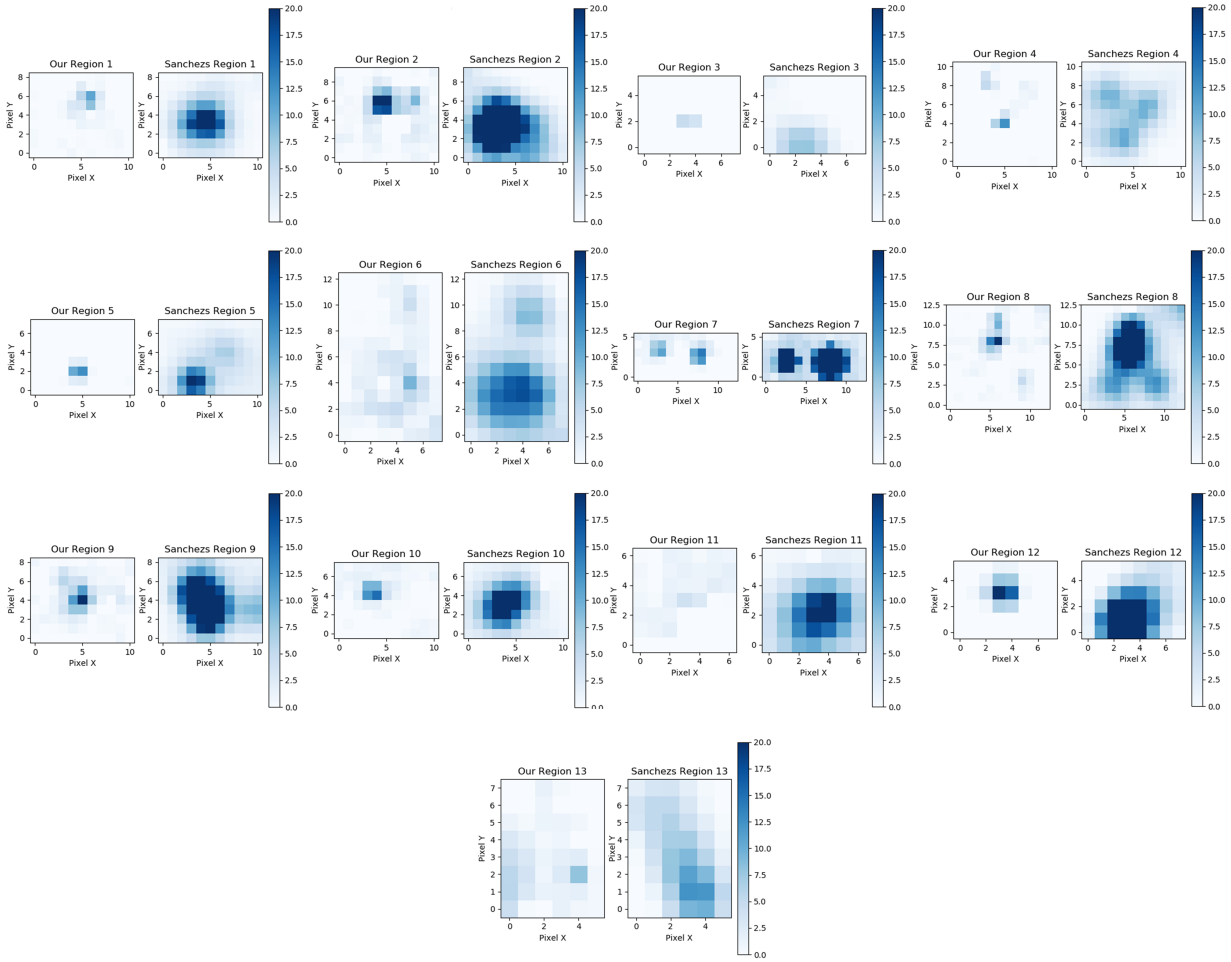

Figure A.1: *Comparison between our Hβ selected regions with the same regions in Sanchez et al. 2010 [25] used to calculate the scale factor.*

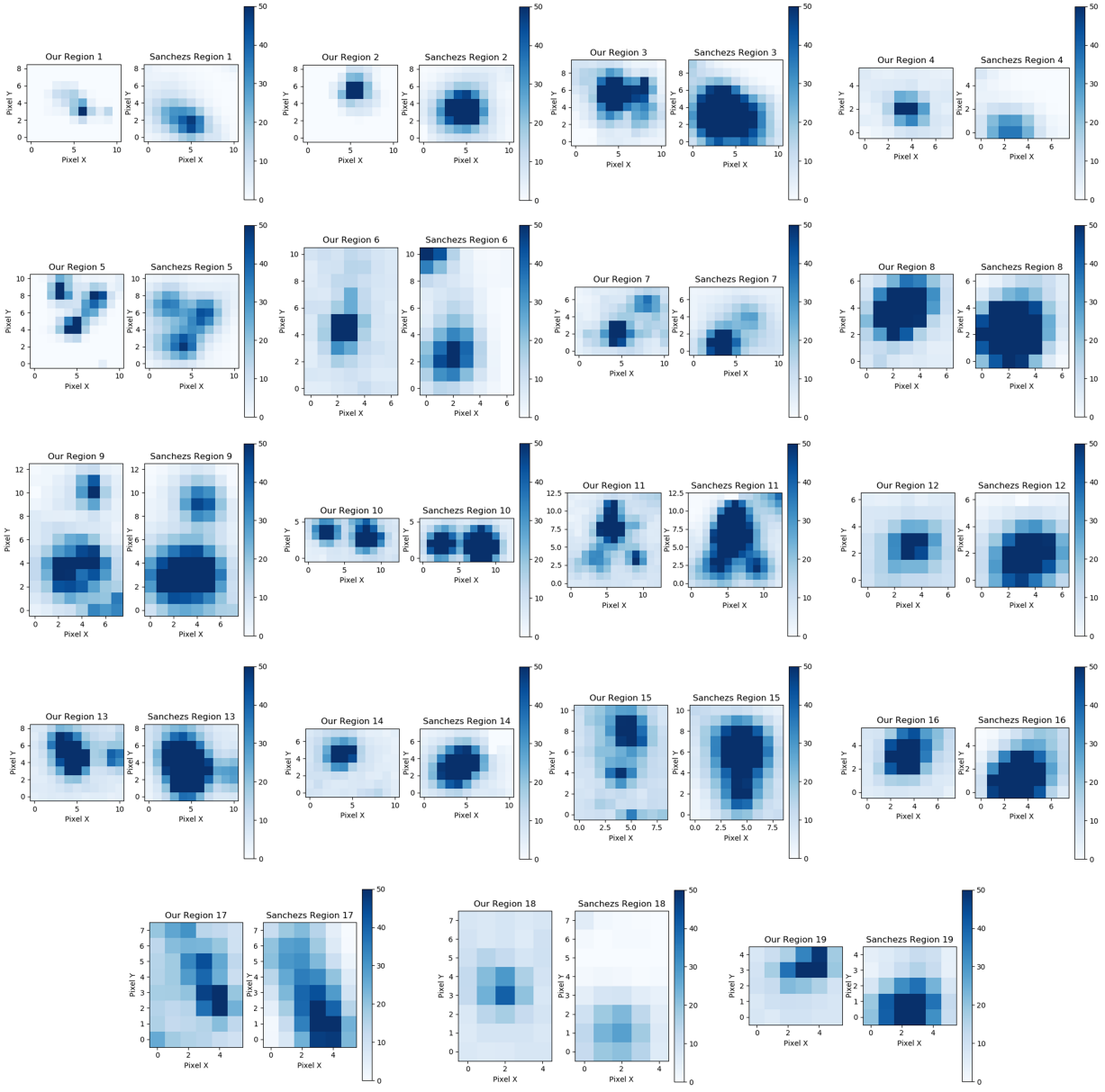

Figure A.2: *Comparison between our Hα selected regions with the same regions in Sanchez et al. 2010 [25] used to calculate the scale factor.*

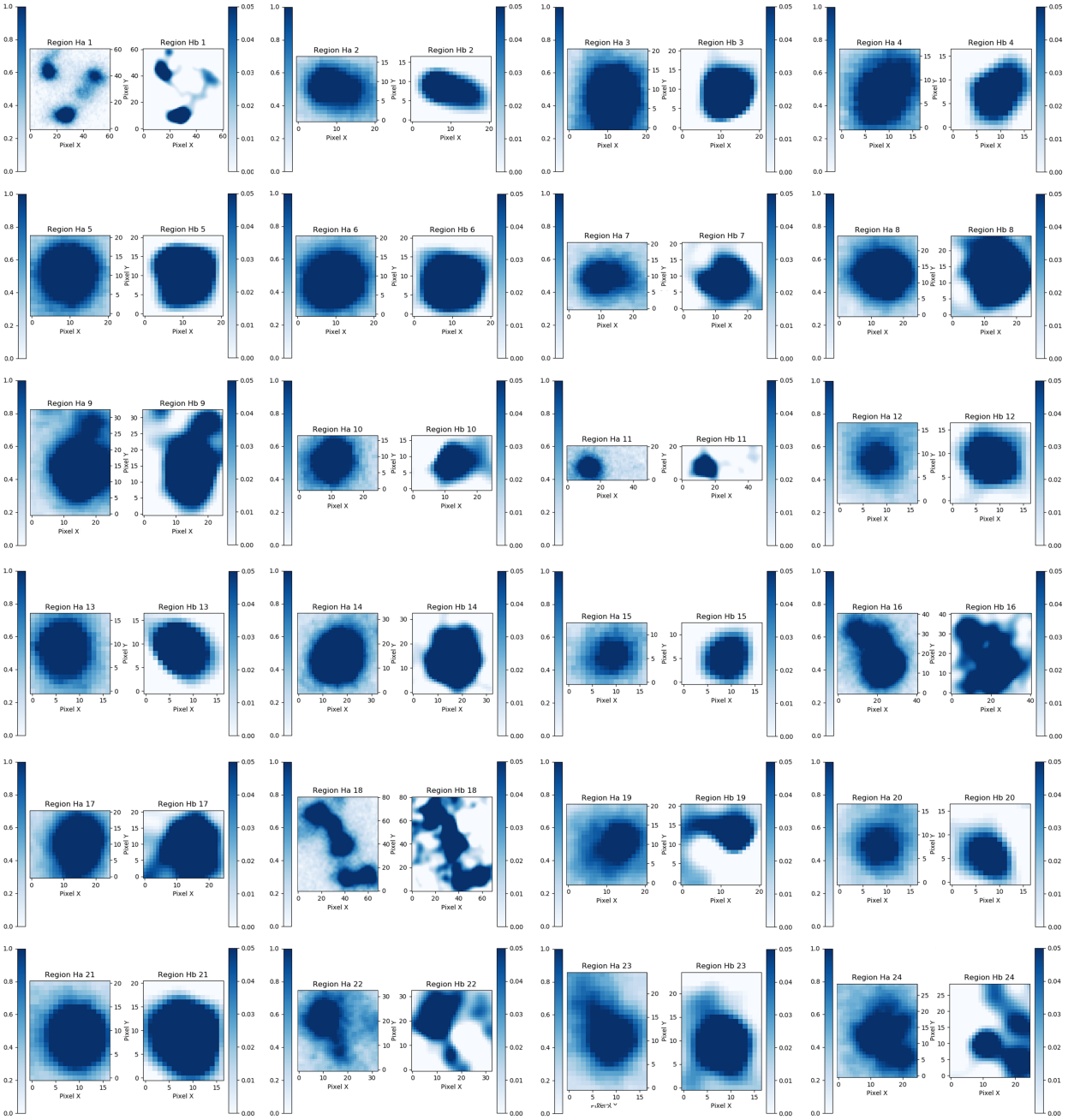
Region Ha 1
Region Hb 1
Region Ha 2
Region Hb 2
Region Ha 3
Region Hb 3
Region Ha 4
Region Hb 4
Region Ha 5
Region Hb 5
Region Ha 6
Region Hb 6
Region Ha 7
Region Hb 7
Region Ha 8
Region Hb 8
Region Ha 9
Region Hb 9
Region Ha 10
Region Hb 10
Region Ha 11
Region Hb 11
Region Ha 12
Region Hb 12
Region Ha 13
Region Hb 13
Region Ha 14
Region Hb 14
Region Ha 15
Region Hb 15
Region Ha 16
Region Hb 16
Region Ha 17
Region Hb 17
Region Ha 18
Region Hb 18
Region Ha 19
Region Hb 19
Region Ha 20
Region Hb 20
Region Ha 21
Region Hb 21
Region Ha 22
Region Hb 22
Region Ha 23
Region Hb 23
Region Ha 24
Region Hb 24
Pixel X
Pixel Y

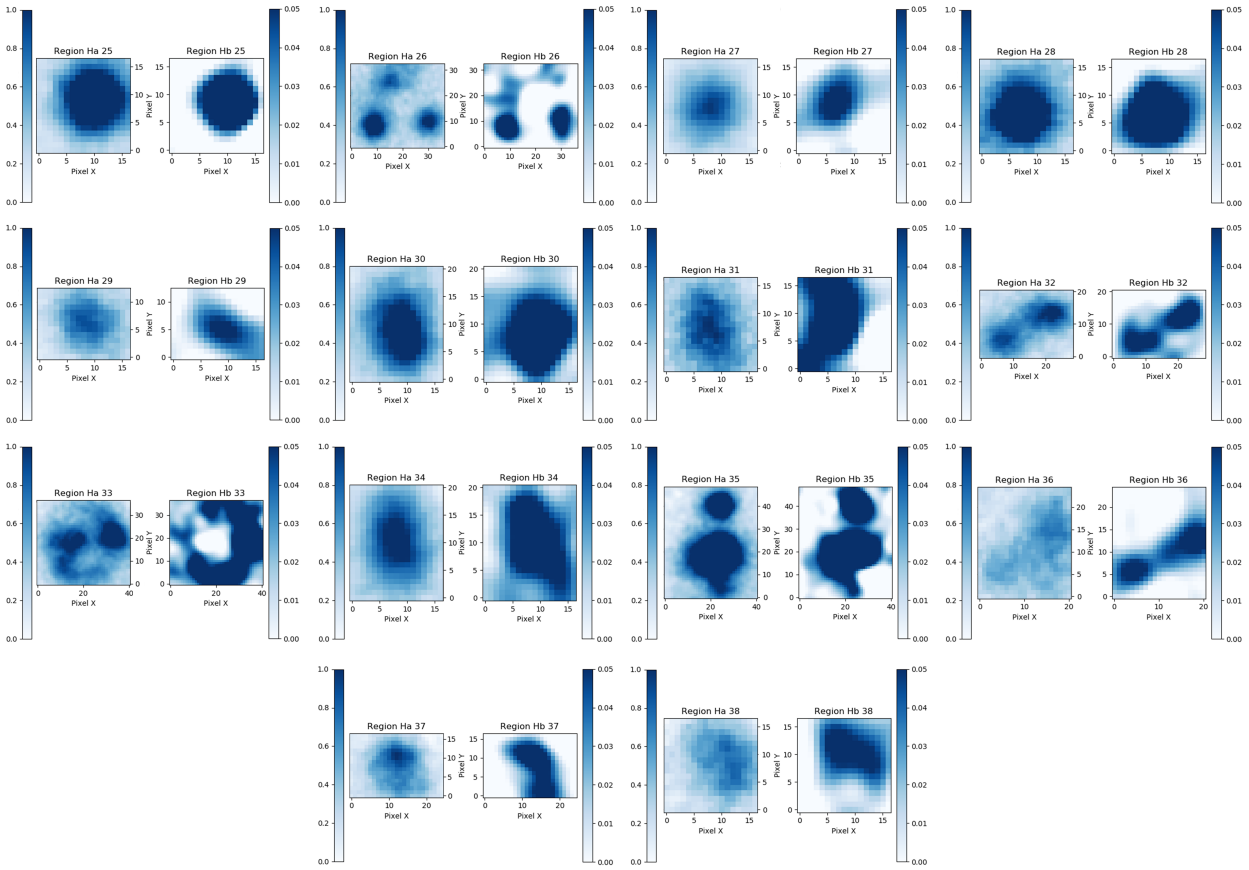

Figure A.3: *Comparison between our Hα and our Hβ selected regions used to calculate the parameters showed in Table 4.1.*